Journal of Fluids and Structures (2002) **16**(2), 247–262
doi:10.1006/jfls.2001.0417, available online at http://www.idealibrary.com on IDEAL®

MECHANISM OF MODE SELECTION FOR TAYLOR VORTEX FLOW BETWEEN COAXIAL CONICAL ROTATING CYLINDERS

M. N. Noui-Mehidi, N. Ohmura and K. Kataoka

Department of Chemical Science and Engineering, Kobe University, Rokkodai, Nada Kobe 657-8501, Japan

(Received 30 June 2000, and in final form 9 July 2001)

A combined numerical and experimental investigation was conducted to study mode selection in Taylor-vortex flow (TVF) between coaxial conical cylinders (truncated cones), where the inner cylinder rotates and the outer one is at rest. Simulations, using a finite-difference method with simplified marker and cell (SMAC) formulation, confirmed the same dependence of mode selection on the acceleration rate β of the inner conical cylinder as observed experimentally. Different TVF modes were obtained in the Reynolds number (Re) range studied. Three different modes corresponding to six, seven and eight pairs of steady Taylor vortices were obtained when the inner conical cylinder rotation speed was increased linearly at different acceleration rates. The transition diagram obtained by Re-β mapping successfully summarizes the various flow states and modes observed.

1. INTRODUCTION

Since the pioneering work of G.I. Taylor (1923), the flow in the annulus between two coaxial rotating cylinders has been the subject of deep investigation devoted to the initial and boundary effects on the annular flow structure (Coles 1955; Andereck *et al.* 1987). Research interest in this system has grown along with its different practical applications in mechanical and chemical engineering (Kataoka 1998). Owing to the variety of the flow configurations studied and the particularity of the transition from the laminar to the turbulent state, the Taylor–Couette flow system is widely considered as a typical model system of routes towards chaos (Cognet 1984).

Recently, from the point of view of hysteresis, more attention has been given to initial conditions and to the way to attain steady rotation of the inner cylinder. Lim *et al.* (1998) reported a new kind of flow pattern in the Taylor–Couette system for different acceleration rates β of the inner cylinder. This state, represented by a flow configuration similar to the Taylor vortex flow, occurs in the Reynolds number range where the wavy vortex flow regime is normally expected. Previously, Burlkhalter & Koschmieder (1974) discovered the initiation of a Taylor-vortex flow (TVF) regime at Reynolds numbers higher than the critical value, Re_c.

The occurrence of Taylor vortices between two rotating spheres has also been numerically and experimentally investigated (Wimmer 1976; Bonnet & De Roquefort 1976). As another variant of the Taylor–Couette system, the flow between two rotating conical cylinders, was also studied (Wimmer 1995; Noui-Mehidi & Wimmer 1999; Hoffmann & Busse 1999). As distinct from circular cylinders, the conical cylinders have the advantage that the Reynolds number changes axially as the radii vary axially also.

0889–9746/02/020247 + 16 $35.00/0

Early studies on the flow between conical cylinders (truncated cones) showed the flow to be highly sensitive to both geometrical and initial conditions. Wimmer (1995) discussed the dependence of the three-dimensional basic flow on the angular velocity, apex angle, axial position and gap width. The conditions leading to the generation of Taylor vortices were also investigated. Noui-Mehidi & Bouabdallah (1993) investigated the laminar–turbulent transition by the use of an electrochemical method and showed that the friction coefficient varied axially. Noui-Mehidi & Wimmer (1999) studied the flow structure observed in the presence of a free surface. Flow configurations supposed to appear only between counter-rotating cylinders have been observed in the conical system with a free surface, even with the outer conical cylinder at rest. Based on numerical computations, Hofmann & Busse (1999) discussed the transition from Taylor-vortex instabilities to Ekman-type instabilities when the apex angle of the conical cylinders is varied.

The present work focuses on the generation of Taylor vortices and its dependence on the acceleration rate of the inner conical cylinder rotation. In both numerical and experimental work, the inner conical cylinder rotation is linearly increased, until the final rotational speed is reached. A transition diagram is drawn by mapping Re versus β to summarize the different flow states and modes observed in the Reynolds range $0 \leq \mathrm{Re} < 1000$ and the acceleration rate range $0{\cdot}06 \leq \beta \leq 1{\cdot}32\ \mathrm{rad/s^2}$.

2. NUMERICAL METHOD

The incompressible Navier–Stokes and continuity equations expressed in cylindrical coordinates with radial (r), azimuthal (θ) and axial (z) components of velocity as shown in Figure 1 are

$$\frac{\mathrm{D}u}{\mathrm{D}t} - \frac{v^2}{r} = -\frac{\partial P}{\partial r} + \frac{1}{\mathrm{Re}}\left(\Delta u - \frac{u}{r^2}\right), \tag{1}$$

$$\frac{\mathrm{D}v}{\mathrm{D}t} + \frac{uv}{r} = \frac{1}{\mathrm{Re}}\left(\Delta v - \frac{v}{r^2}\right), \tag{2}$$

$$\frac{\mathrm{D}w}{\mathrm{D}t} = -\frac{\partial P}{\partial z} + \frac{1}{\mathrm{Re}}\Delta w, \tag{3}$$

$$\frac{1}{r}\frac{\partial (ru)}{\partial r} + \frac{\partial w}{\partial z} = 0. \tag{4}$$

Previous flow visualization observations have shown that the observed steady Taylor vortices are axisymmetric (Wimmer 1995; Noui-Mehidi & Wimmer 1999). The governing equations (1)–(4) are presented here in a conservative form, where the derivatives with respect to θ are neglected due to the assumption of axisymmetry. These equations require the solution for the pressure P and the three components of velocity u, v and w in the directions r, θ and z, respectively. The derivative operators in equations (1)–(4) are

$$\frac{\mathrm{D}}{\mathrm{D}t} = \frac{\partial}{\partial t} + \frac{1}{r}\frac{\partial (ru)}{\partial r} + \frac{\partial w}{\partial z}, \tag{5}$$

$$\Delta = \frac{1}{r}\frac{\partial}{\partial r}\left(r\frac{\partial}{\partial r}\right) + \frac{\partial^2}{\partial z^2}. \tag{6}$$

In this framework, the Reynolds number is given by

$$\mathrm{Re} = \frac{R_{ih}\Omega d}{\nu}, \tag{7}$$

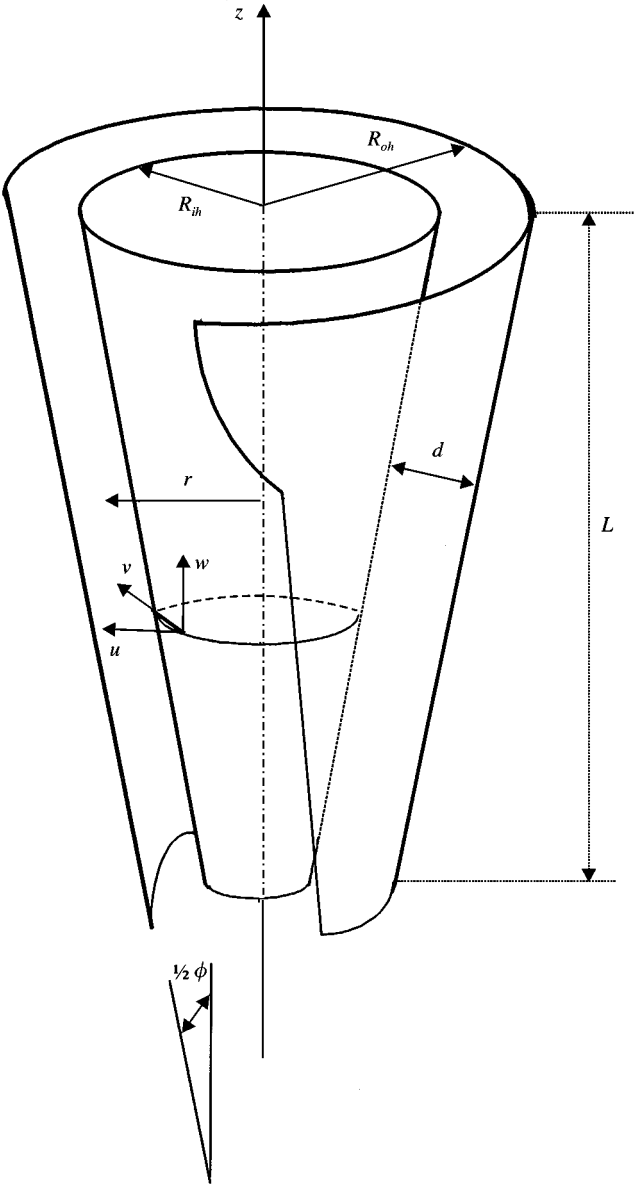

Figure 1. Flow system and notation.

where R_{ih} is the maximum radius of the inner conical cylinder, d the gap width, Ω the angular velocity and ν the kinematic viscosity.

The boundary conditions on the conical walls cannot be easily expressed in cylindrical coordinates. This problem can be avoided by adopting the following coordinate-transformation function (Noui-Mehidi *et al.* 1999):

$$f: \begin{aligned} \eta &= r - z\tan\alpha, \\ \xi &= z. \end{aligned} \tag{8}$$

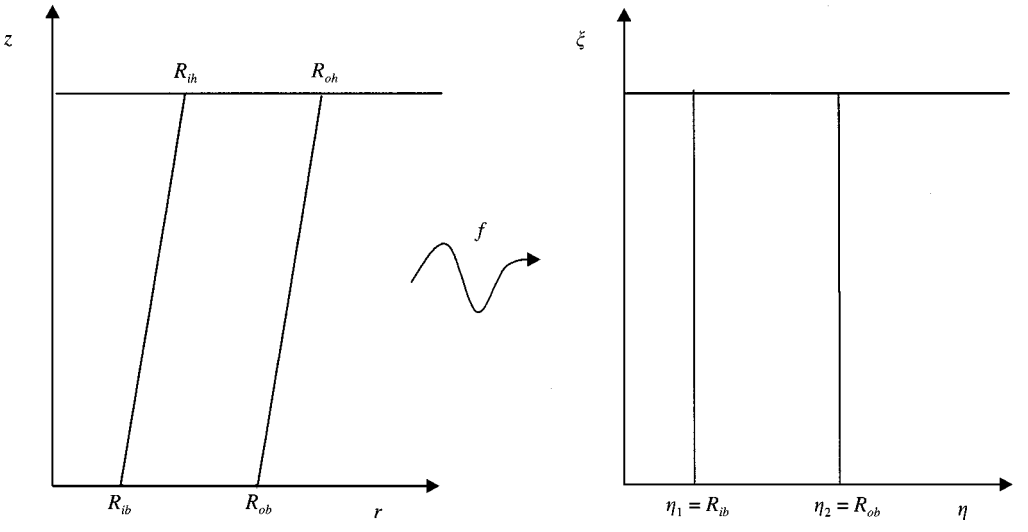

Figure 2. Coordinate transformation. Left: physical domain; right: numerical domain.

This function transforms the physical domain (r, z) to a numerical one (η, ξ), as shown in Figure 2. The transformed boundary conditions become constant on the walls.

Replacing the partial derivatives in equations (1)–(4) with the corresponding derivatives in the (η, ξ) domain leads to the following system of equations:

$$\frac{\mathrm{D}u}{\mathrm{D}t} - \frac{v^2}{\eta + \xi \tan\alpha} = -\frac{\partial P}{\partial \eta} + \frac{1}{\mathrm{Re}}\left[\Delta u - \frac{u}{(\eta + \xi \tan\alpha)^2}\right], \tag{9}$$

$$\frac{\mathrm{D}v}{\mathrm{D}t} + \frac{uv}{\eta + \xi \tan\alpha} = \frac{1}{\mathrm{Re}}\left[\Delta v - \frac{v}{(\eta + \xi \tan\alpha)^2}\right], \tag{10}$$

$$\frac{\mathrm{D}w}{\mathrm{D}t} = -\frac{\partial P}{\partial \xi} + \tan\alpha \frac{\partial P}{\partial \eta} + \frac{1}{\mathrm{Re}}\Delta w, \tag{11}$$

$$\frac{\partial u}{\partial \eta} + \frac{u}{\eta + \xi \tan\alpha} + \frac{\partial w}{\partial \xi} - \tan\alpha \frac{\partial w}{\partial \eta} = 0, \tag{12}$$

where the derivative operators become

$$\frac{\mathrm{D}}{\mathrm{D}t} = \frac{\partial}{\partial t} + \frac{\partial u}{\partial \eta} + \frac{u}{\eta + \xi \tan\alpha} - \tan\alpha \frac{\partial w}{\partial \eta} + \frac{\partial w}{\partial \xi}, \tag{13}$$

$$\Delta = (1 + \tan^2\alpha)\frac{\partial^2}{\partial \eta^2} + \frac{1}{\eta + \xi \tan\alpha}\frac{\partial}{\partial \eta} - 2\tan\alpha \frac{\partial^2}{\partial \eta \partial \xi} + \frac{\partial^2}{\partial \xi^2}. \tag{14}$$

If the apex angle α is set to zero, the system of equations (9)–(12) reduces to the system for the classical Taylor–Couette flow corresponding to equations (1)–(4).

In the transformed numerical domain, the boundary conditions corresponding to the no-slip conditions at the walls are

$$\begin{aligned} &\eta = \eta_1, \quad u = w = 0, \quad v = 1, \\ &\eta = \eta_2, \quad u = v = w = 0. \end{aligned} \tag{15}$$

The simplified marker and cell (SMAC) formulation developed by Amsden & Harlow (1970) is employed in the numerical simulation of the generation of vortices. The momentum and continuity equations are solved using a staggered mesh discretization in space with equal interval grids in the η and ξ directions (Fletcher 1991). A first-order time-integration scheme is then applied, with central finite differences for spacial discretization. A Poisson's equation solver is developed to solve the equation of an auxiliary velocity potential function ϕ defined in equation (16),

$$u = \frac{\partial \phi}{\partial r}, \quad v = \frac{\partial \phi}{\partial z}. \tag{16}$$

In the resulting Poisson's equation, the point SOR method is used together with the concept of the SMAC formulation to directly satisfy the condition of continuity of the potential function ϕ.

The acceleration of the rotation of the inner conical cylinder was simulated numerically by changing the rotational boundary condition from zero, until the final rotation is reached. A linear acceleration path is followed with a constant acceleration rate defined by (Ohmura *et al.* 1994)

$$\beta = \frac{\Delta \Omega}{\Delta t}. \tag{17}$$

The solution is integrated forward in time, until the flow becomes steady for the desired Reynolds number and acceleration rate. A direct comparison between the simulations and the experimental observations can be made in terms of the Reynolds number and acceleration rate β.

At present, the apex angle in the experimental apparatus cannot be varied. The dependence of the Reynolds number on the apex angle will therefore be investigated in the next phase.

3. EXPERIMENTAL CONDITIONS

The experimental set-up, shown in Figure 3, consists of a vertical, rotating inner cone made of stainless steel with an upper radius $R_{ih} = 42$ mm and a transparent stationary outer cone made of Plexiglas with an upper radius $R_{oh} = 50$ mm. Both conical cylinders have the same apex angle, $\phi = 16^\circ$, so that the gap width is kept axially constant, $d = 8$ mm. At the top of the flow system, the radius ratio is then $\chi = R_{ih}/R_{oh} = 0{\cdot}840$. Both top and bottom plates are fixed to the outer cone. The fluid column height is $L = 125$ mm, which gives an aspect ratio $\Gamma = L/d = 15{\cdot}62$. The working fluid is an aqueous solution of 66 vol% glycerol; 2% of Kalliroscope AQ1000 is added for flow visualization. The fluid temperature is measured by the use of a thermocouple (Copper/Constantan), with an accuracy of $0{\cdot}1^\circ$C. The kinematic viscosity is 14·81 cS at 25°C. The visualized flow structure is recorded with a high-resolution video camera. Two illumination techniques are utilized: (i) Argon laser sheet illumination for observing a cross-section of the gap, and (ii) reflected white light illumination for the observation of the front view of the flow system. The inner cone rotation speed is controlled by a computer program. In the start-up operation, the cylinder rotation is accelerated linearly, following

$$\Omega(t) = \beta t. \tag{18}$$

until the final speed for the specified steady state is reached. The acceleration procedure has been described by many authors as a quasi-static acceleration of the inner cylinder

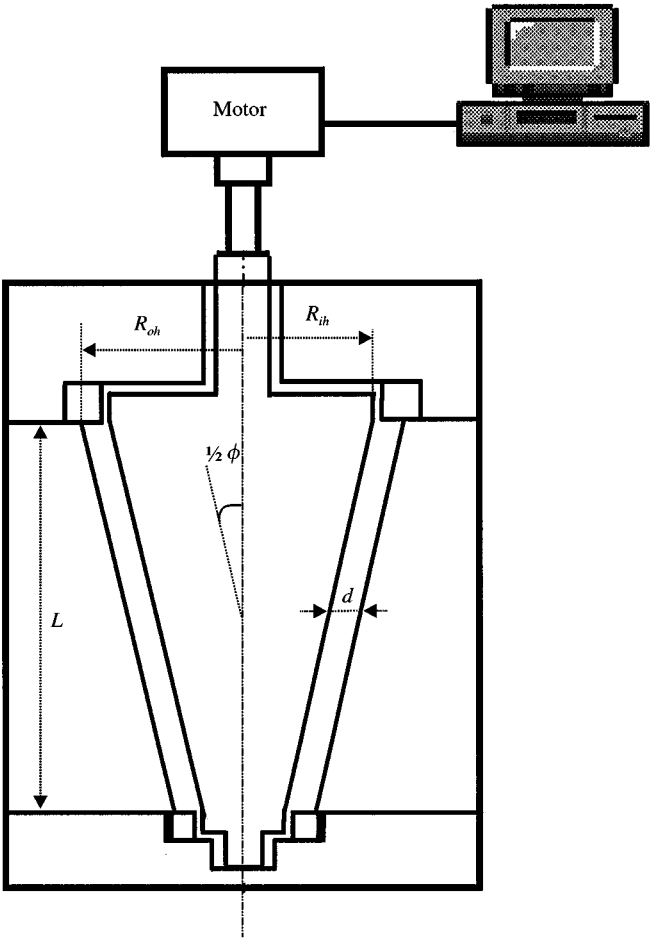

Figure 3. Experimental apparatus and arrangement.

(Andereck *et al.* 1986). Once the target Reynolds number is set, the inner cone is slowly accelerated from rest with a constant rate β, until the final target rotation is reached. The visualization recordings of steady-state flow are done after a time equivalent to over a 100 times the acceleration time, i.e., when the flow is steady. As stated in Section 1, the acceleration rate β is varied between 0·06 and 1·32 rad/s^2.

4. RESULTS AND DISCUSSION

4.1. Appearance of The First Taylor Vortices

The basic flow in the present system is three-dimensional. The flow structure depends on the apex angle, gap width, angular velocity and axial position, as reported by Wimmer (1995). In addition to the tangential and radial motions, the meridional or axial flow influences the hydrodynamics of this system. In a cross-section of the gap width, the meridional motion is upward along the wall of the rotating inner cone, and downward along the wall of the fixed outer cone.

On increasing the angular velocity of the inner cone from rest, with a constant acceleration rate β, the balance between the centrifugal and viscous forces is lost at the first critical Reynolds number Re_c. The instability due to the centrifugal effect is maximal at the largest radii and leads to the occurrence of the first Taylor vortex near the top of the flow system observed experimentally at $\mathrm{Re}_c = 132$.

The first observed vortex has a radially inward flow along the end plate, i.e., counter-rotating to the meridional flow. As an illustration of this flow state, the simulation in Figure 4 shows the formation of the first single vortex at Re_c near the top of the flow system, while the

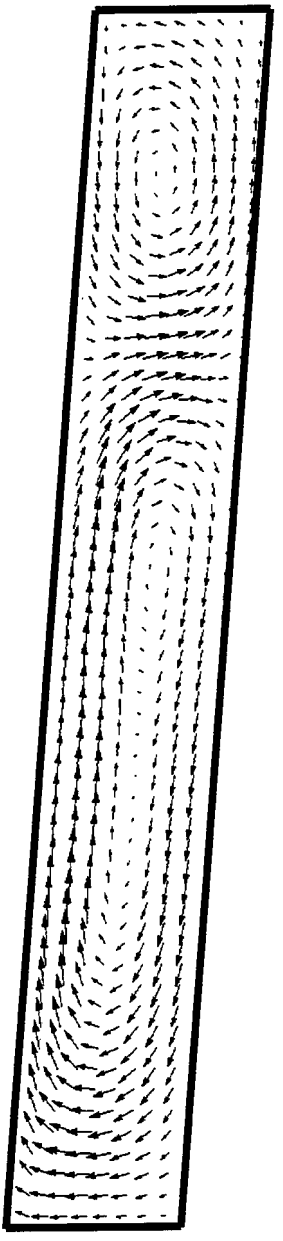

Figure 4. Numerical simulation for the appearance of the first vortex for $\beta = 0{\cdot}09$ and $\mathrm{Re} = 134$.

rest of the fluid follows the meriodional motion. As can be seen, in the lower part, the velocity of the meriodional flow motion is higher near the rotating inner cone wall than in the vicinity of the stationary outer cone wall.

Increasing further the angular velocity of the inner cone, more vortices are generated, one below the other. The second vortex rotates in the direction opposite to the first one, following the rotation sense of the meridional flow as, seen in the simulation of Figure 5(b). The region separating the second vortex from the meriodional flow in the cross-section of the gap is not clear, since the second vortex and the meriodional flow rotate in the same sense. This property cannot be observed experimentally, owing to the very slow secondary motion. As can be seen in Figure 5(b), this separation region is considerably wide. The region where the

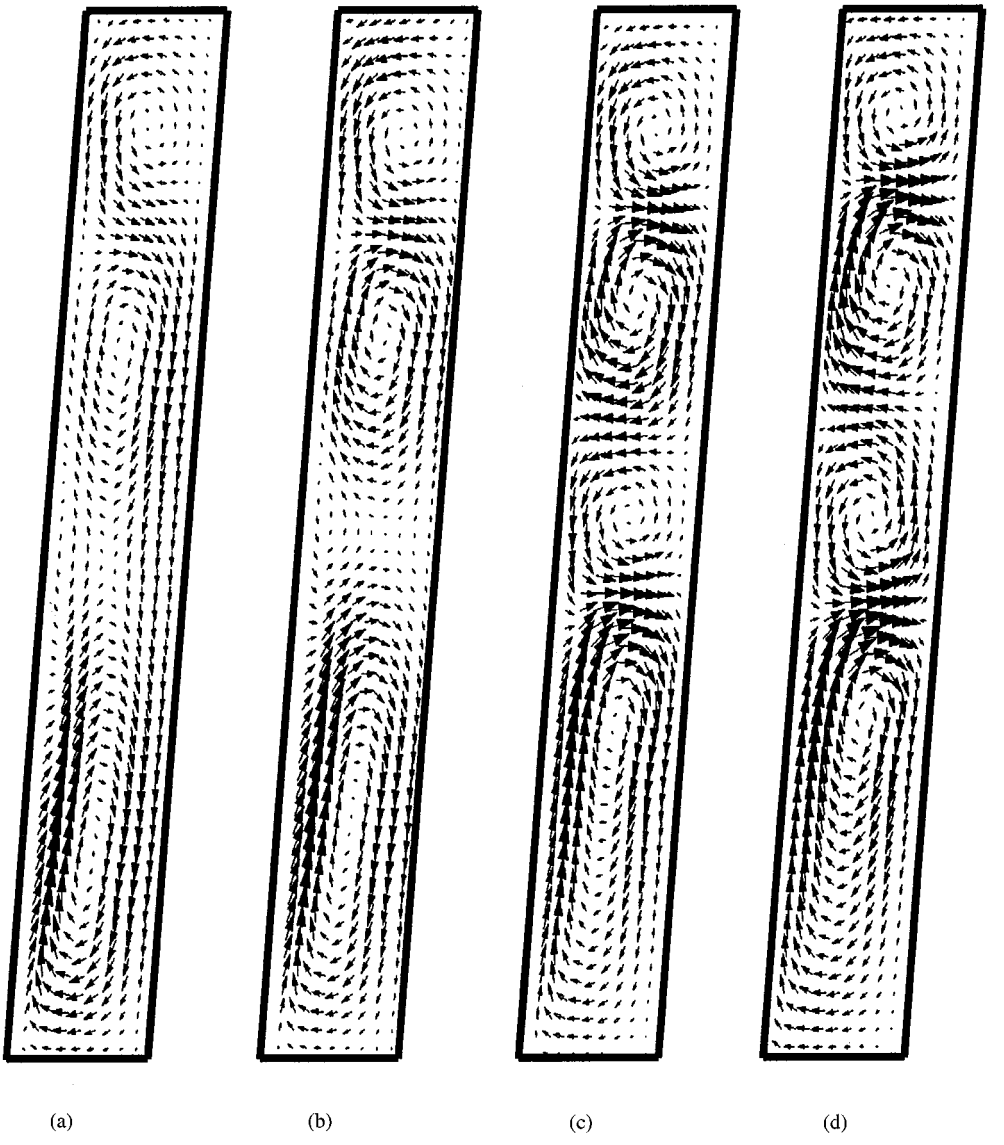

Figure 5. Numerical simulations of the generation sequences for the first vortices at $\beta = 0{\cdot}09$: (a) Re = 142, (b) Re = 150, (c) Re = 158 and (d) Re = 166.

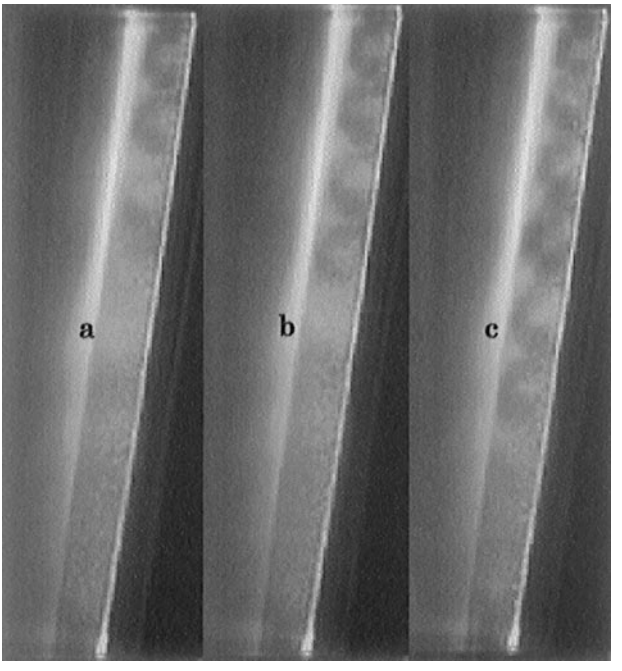

Figure 6. Laser sheet visualization of the first vortices for $\beta = 0{\cdot}12$: (a) Re = 170, (b) Re = 182 and (c) Re = 190.

fluid layers coming from the second vortex and the meridional motion merge can be regarded as a dead zone since the secondary motion is very weak.

All the generated vortices are horizontal and counter-rotating, two by two from the top. The numerical simulation results of Figure 5 clearly represent the generation sequence of these vortices. In the simulations, β is kept constant while the Reynolds number is slowly increased above the critical value. The laser sheet visualization displayed in Figure 6 also clearly shows the sequence of the generation of the first vortices. As can be seen in Figure 6(c), in the gap, the top vortices already have a strong motion represented by dark zones, whereas new vortices generated below in the lower part have weak motions identified as lighter zones. In the same figure, it is seen that the sizes of the vortices vary axially along the fluid column.

4.2. Upward Travelling Vortices

Increasing further the angular velocity of the inner cone, at Re = 193, three-quarters of the fluid column is filled with vortices, as observed experimentally. At this stage, the vortices, still horizontal, begin to move upwards heading for the largest radius. This motion is due to the strong meridional motion at the bottom of the system where the flow is still basic.

At Re = 209, the whole fluid column is filled with upwards travelling vortices as more vortices appear in the residual-free lower part. A periodic phenomenon is observed as a new vortex is generated periodically at the bottom of the fluid column. This vortex travels upward, until it disappears, crashing on the uppermost top vortex which remains with a strong vorticity.

Experimentally, the velocity c of this upward motion is evaluated based on the elapsed time between the birth of a vortex at the bottom and its disappearance at the top of the flow

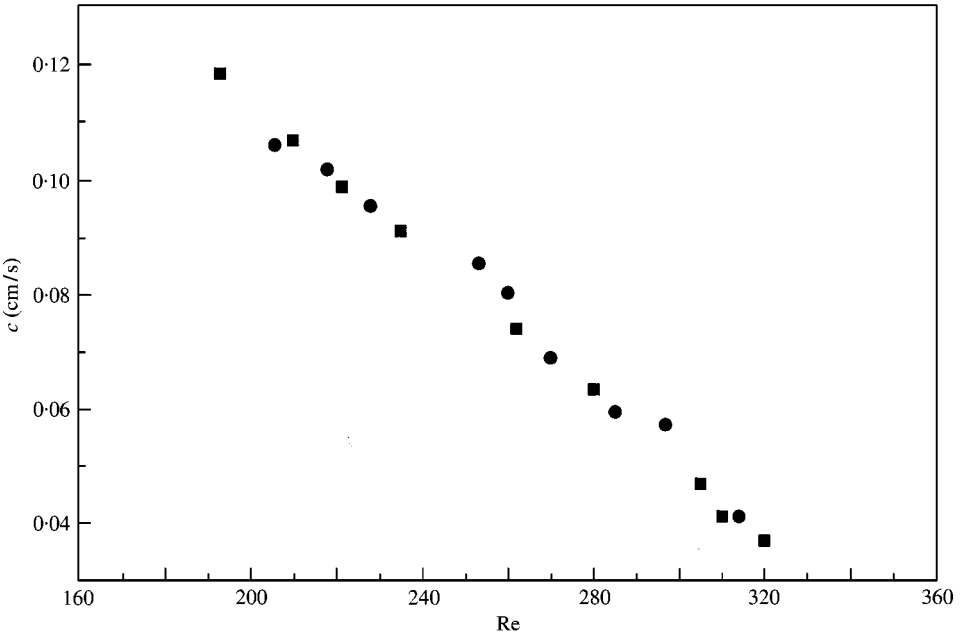

Figure 7. Velocity of the upward motion versus Reynolds number for different β: ■, $\beta = 0{\cdot}3$; ●, $\beta = 0{\cdot}5$.

system. As shown in Figure 7, this velocity decreases linearly with a slope of 0·014 when the Reynolds number increases. It should also be noted that the upward motion does not depend on the acceleration rate β. Finally, the upward motion stops and steady Taylor vortices are then observed at Re = 320. As will be described in Section 4.3, depending on the value of β, vortex modes with six, seven or eight pairs of vortices are observed in the fluid column in the final state.

4.3. Steady Toroidal Vortices

The final state is reached after the upward motion stops and steady horizontal toroidal vortices are established in the flow system. This steady state is nonunique and depends on the acceleration rate β. Configurations of six, seven or eight pairs of vortices can be observed, depending on the history leading up to the steady flow state. The nonuniqueness of the flow modes has been discussed by some authors in the case of circular rotating cylinders (Coles 1965; Burkhalter & Koschmieder 1974) and in the case of rotating conical cylinders (Wimmer 1995). In Figures 8·1, 8·2 and 8·3, the configurations of six, seven and eight pairs of vortices are confirmed both numerically and experimentally. The numerical simulations [Figures 8·1(b), 8·2(d) and 8·3(f)] show the same axial disposition of the steady vortices as observed in the three modes for the corresponding experimental conditions. The size of the vortices decreases from the bottom to the top of the flow system. The vortices are coupled as a pair of large and small counter-rotating vortices. As also noticed from the three photographs presented in Figures 8·1(a), 8·2(c) and 8·3(e), in all the observed steady states the sizes of the large and small cells even vary from one axial position to the other. The vortex at the bottom of the flow system is larger than the one at the top. It has been confirmed by numerical simulations that it is the large vortices which rotate in the same sense as the meriodional flow. The small vortices are counter-rotating to the meriodinal flow with a vorticity weaker than that of the larger vortices.

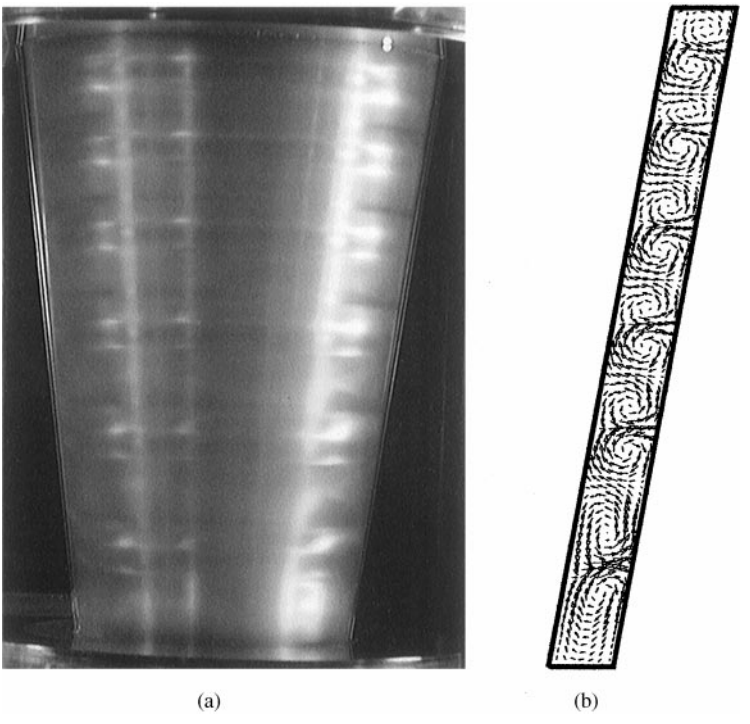

Figure 8.1. Configuration of six pairs of steady vortices ($\beta = 0{\cdot}6$, Re $= 340$): (a) flow visualization; (b) numerical simulation.

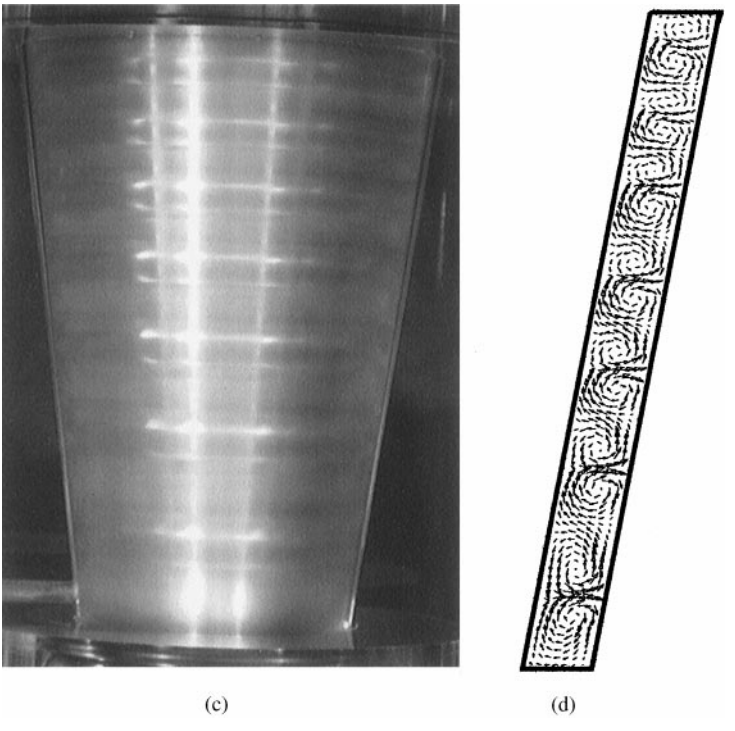

Figure 8.2. Configuration of seven pairs of steady vortices ($\beta = 1{\cdot}3$, Re $= 520$): (c) flow visualization; (d) numerical simulation.

doi:10.1006/jfls.2001.0417

For the case of six pairs of Taylor vortices, a time sequence of the evolution from the birth of the first vortices to the final steady state obtained by numerical simulations is shown in Figure 9(a–d). The steady state, Figure 9(d), is reached after the calculation time $\tau^* = \tau$ for a Reynolds number $\mathrm{Re} = 373$ and an acceleration rate $\beta = 0{\cdot}8$. The first sequence, Figure 9(a), corresponds to a calculation time of $\tau/30$ and represents the appearance of the first vortices. At $\tau^* = \tau/20$ [Figure 9(b)], more vortices are formed gradually. The transient state, Figure 9(c), obtained for $\tau^* = \tau/15$ has 13 cells, and the dimensions of the vortices are smaller than in the steady state [Figure 9(d)]. This state, obtained numerically, is transient due to the existence of an odd number of vortices. Only in the upward-motion flow-state can the same number of cells be seen, because of the axial movement. The final steady state [Figure 9(d)] has 12 vortices, similar to what is observed experimentally as stated with regard to Figure 8.1.

Since the vortices are different in size axially, i.e., the wavelength varies along the fluid column, the definition of the wavelength is quite delicate. As the vortices are formed axially alternately large and small, the wavelength can be defined classically, based on a vortex pair: the wavelength λ is then the axial length occupied by a pair of adjacent large and small counter-rotating vortices. The mid-point of an imaginary line joining the vortex centers is taken as the axial location for both numerical and experimental observations. In Figure 10, the nondimensional axial wavelengths λ^*, defined by $\lambda^* = \lambda/L$, are displayed for different axial locations. The first pair of vortices is formed by the large vortex at the bottom and the next upper small vortex. As noticed in Figure 10, for the six-pair and seven-pair modes, the relative difference of size between experimental observations and numerical simulations lies in the range 1–10%. In the case of eight pairs of vortices, the difference is between 3 and 30%. For the same experimental conditions, the simulations permitted to obtain a configuration with eight pairs of vortices. The difference in size is probably attributable to numerical effects, since the calculation time is shorter than in the six-pair and the seven-pair cases. That configuration can only be obtained for high Reynolds numbers and high acceleration rates will be discussed in the following section.

On the other hand, it is found, both numerically and experimentally, that the wavelength decreases axially from the bottom to the top of the flow system, except near the upper end plate.

In the case of very small acceleration rates of the rotating inner cone, the different flow modes observed can be mapped as in Figure 11. As stated earlier, the procedure involves first fixing the final angular velocity to be reached and then accelerating, linearly, the rotation of the inner cone from rest, with different acceleration rates. All the observed structures are confined in a limited number of specific regions depending on Re and β. In Figure 11, the range of Reynolds number ($320 \leq \mathrm{Re} \leq 850$) where the steady toroidal vortices appear is not in regular square form. This hysteretic dependence is clearly explained by Figure 12. Different flow modes appear within the regions of steady vortex flow.

It is apparent that the most preferred vortex configuration within the present flow system is the TVF mode with seven pairs of vortices, occupying the widest region in Figure 12. At a given Reynolds number, two different steady-state configurations can be established, depending on the acceleration rate. Two different flow modes having six and seven pairs of vortices, respectively, are observed simultaneously at low Reynolds numbers. Although the six-pair mode is observed for small β, the seven-pair mode occurs for greater β, for the same Reynolds number. Two different flow modes, having seven and eight pairs of vortices, respectively, are also observed simultaneously at higher Reynolds numbers. The eight-pair mode is obtained for greater β than the seven-pair mode for the same Reynolds number.

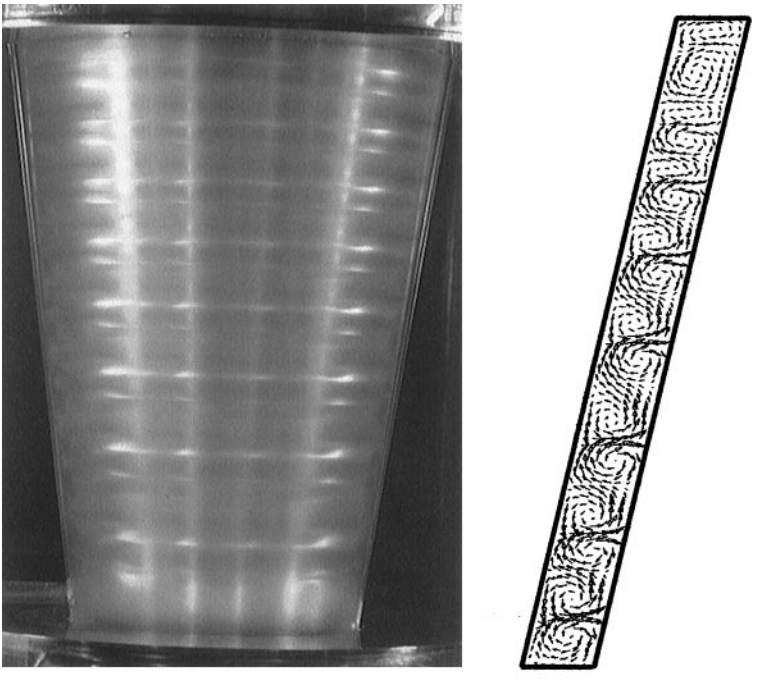

Figure 8.3. Configuration of eight pairs of steady vortices ($\beta = 1{\cdot}3$, Re $= 730$): (e) flow visualization; (f) numerical simulation.

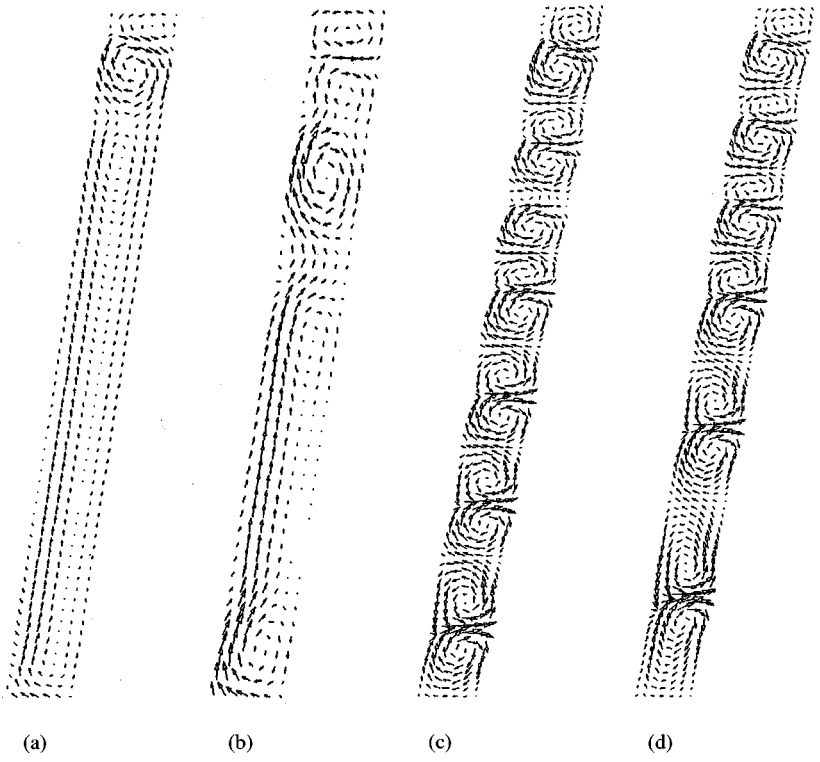

Figure 9. Time sequence transition to the steady state for Re $= 373$ and $\beta = 0{\cdot}8$: (a) $\tau^* = \tau/30$; (b) $\tau^* = \tau/20$; (c) $\tau^* = \tau/15$ and (d) $\tau^* = \tau$.

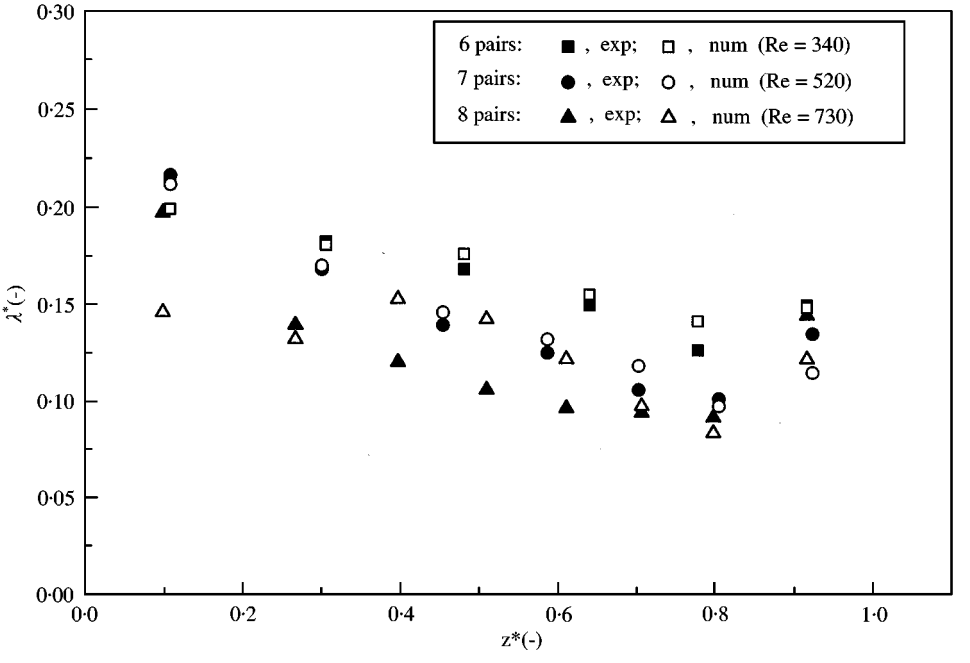

Figure 10. Axial wavelength of the toroidal vortices in the axial direction z for both numerical and experimental results.

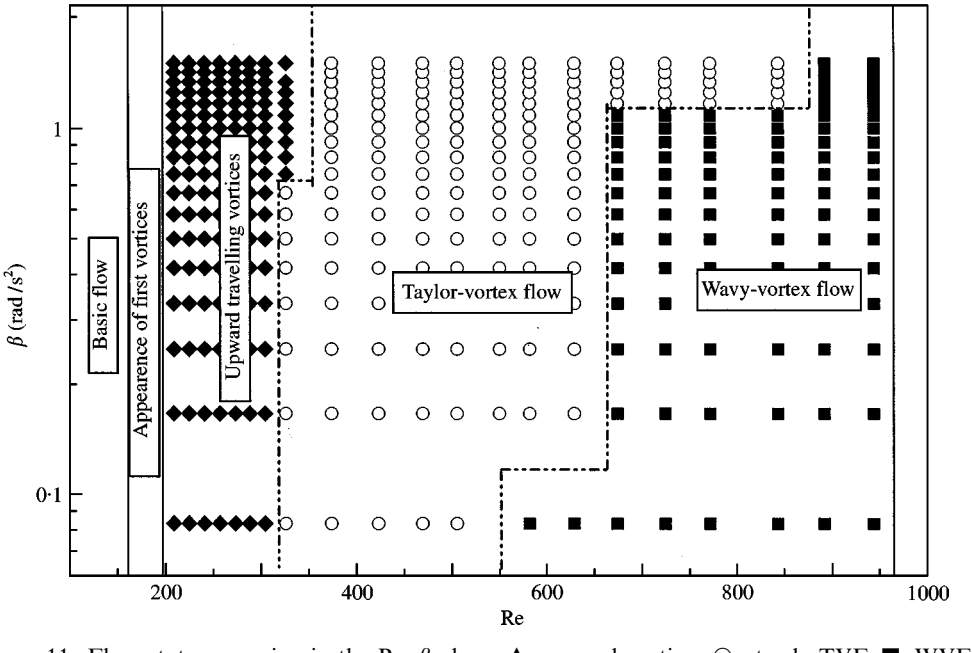

Figure 11. Flow states mapping in the Re–β plane: ▲, upward motion; ○, steady TVF; ■, WVF.

However, the three modes cannot coexist at a given Reynolds numbers. This mode selection is shown in Figure 13. At some Reynolds numbers, where two modes coexist for different values of β, the jump from one configuration to the other occurs at a critical value of β. This critical value depends on the Reynolds number.

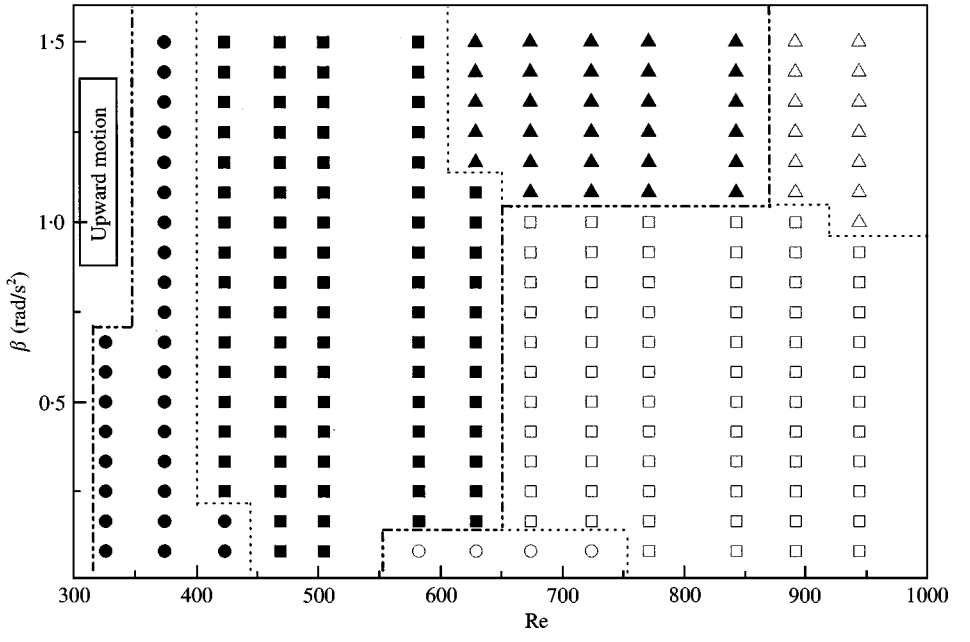

Figure 12. Flow regions of TVF and WVF in the Re–β plane: ●, six pairs of steady vortices; ○, six pairs of wavy vortices; ■, seven pairs of steady vortices; □, seven pairs of wavy vortices; ▲, eight pairs of steady vortices; △, eight pairs of wavy vortices.

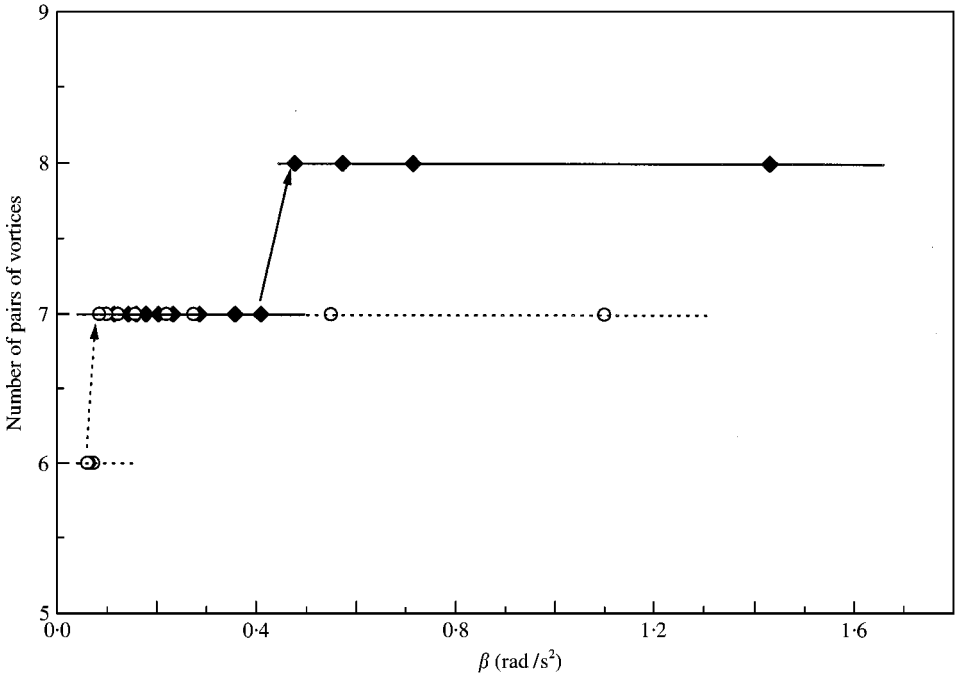

Figure 13. Mode selection as a function of β: ◆, Re = 649; ○, Re = 428.

4.4. Wavy Vortex Flow

In the range of Reynolds numbers investigated ($Re < 1000$), it has also been found that wavy-vortex flow (WVF) appears for higher Reynolds numbers. As in the circular Couette system, the WVF is characterized by the appearance of an azimuthal wave motion which is superimposed on the steady cellular motion. The WVF observed in the present system has the same characteristics as that observed between circular cylinders (Cognet 1984).

According to Figures 11 and 12, flow with either steady vortices or wavy vortices is observed, depending on β for the same Reynolds number. The mode with six pairs of wavy vortices exists in a very narrow region, $550 \leq Re \leq 750$ and $\beta \leq 0{\cdot}08$. Two different modes having, respectively, seven pairs of wavy vortices and eight pairs of steady vortices are also observed in the range $650 \leq Re \leq 750$. Furthermore, in a small range ($600 < Re \leq 750$), three modes can be observed for the same Reynolds number. In one case, three different modes, i.e., six pairs of WVF, seven pairs of TVF and eight pairs of TVF, occur at different β. In another case, another combination of flow modes, i.e., six pairs of WVF, seven pairs of WVF and eight pairs of TFV can also exist, depending on β. For higher Reynolds numbers, $Re > 850$, only seven or eight pairs of WVF are observed.

5. CONCLUSIONS

The present paper dealt with a qualitative and quantitative evaluation of the different conditions leading to the occurrence of Taylor vortices between coaxial conical cylinders. The hydrodynamics of this flow system may be considered to be singular, in the sense that the steady Tayler vortex flow (TVF) is established after an upward travelling motion of the first observed vortices due to the basic three-dimensional flow. Depending on the acceleration rate β of the inner cone rotation, in the TVF state, three different modes with six, seven or eight pairs of vortices are obtained in the present flow system.

The conditions of appearance of these flow modes have successfully been summarized by Re-β mapping. The Re-β flow mode regions have no regular shapes since a combination of flow modes can coexist, even for the same Reynolds number, when β is changed. The numerical simulations have confirmed the various observed flow modes for the same Re-β experimental condition and gave complementary information about the transient flow structures before the steady state is reached.

Modes of Wavy Vortex Flow (WVF) have been obtained from the TVF when the Reynolds number is further increased. Combinations of TVF and WVF modes also coexist for the same Reynolds number for different values of β. In this flow system, the selection of the flow mode to be reached can be controlled by the choice of the acceleration rate.

ACKNOWLEDGEMENTS

The authors would like to thank Dr Njuki Mureithi, Department of Mechanical Engineering, Faculty of Engineering, Kobe University, in matters concerning the editing of the present work.

References

Andereck, C. D., Liu, S. S. & Swiney, H. L. 1986 Flow regimes in a circular couette system with independently rotating cylinders. *Journal of Fluid Mechanics* **164,** 155–183.

Amsden, A. A. & Harlow, F. H. 1970 A simplified MAC technique for incompressible fluid flow calculations. *Journal of Computational Physics* **6,** 322–325.

Bonnet, J. P. & de Roquefort, T. A. 1976 Ecoulement entre deux spheres concentriques en rotation. *Journal de Mécanique* **15,** 373–397.

Burkhalter, J. E. & Koschmieder, E. L. 1974 Steady supercritical Taylor vortex flow after sudden starts. *Physics of Fluids* **17,** 1929–1935.

Cognet, G. 1984 Les étapes vers la turbulence dans l'écoulement de Couette–Taylor entre cylindres coaxiaux. *Journal de Mecanique Theorique et Appliquée*, special Issue, 7–44.

Coles, D. 1965 Transition in circular Couette flow. *Journal of Fluid Mechanics* **21,** 385–425.

Fletcher, C. A. J. 1991 *Computational Techniques for Fluid Dynamics*, Vol. 2. Berlin: Springer-Verlag.

Kataoka, K. 1998 New aspects of instabilities and their bifurcation in transport phenomena with/without chemical reactions. *Institution of Chemical Engineers, Proceedings of CHEMECA*98 Plenary Lecture N6, 28–30 September, Port-Douglas, Australia.

Hoffman, N. P. & Busse, F. H. 1999 Instabilities of shear flows between two coaxial differentially rotating cones. *Physics of Fluids* **11,** 1676–1678.

Lim, T. T., Chew, Y. T. & Xiao, Q. 1998 A new flow regime in a Taylor–Couette system. *Physics of Fluids* **10,** 3233–3235

Noui-Mehidi, M. N. & Bouabdallah, A. 1993 Laminar turbulent transition in the flow confined between rotating coaxial cones. *Proceedings of third International Workshop Electrodiffusion Diagnostics of Flows*, Dourdan, France, 9–12 May, pp. 139–147.

Noui-Mehidi, M. N. & Wimmer, M. 1999 Free surface effects on the flow between conical cylinders. *Acta Mechanica* **135,** 13–25.

Noui-Mehidi, M. N., Salem, A., Legentilhomme P. & Legrand, J. 1999 Apex angle effects on the swirling flow between cones induced by means of a tangential inlet. *Journal of Heat and Fluid Flow* **20,** 405–413.

Ohmura, N., Kataoka, K., Kataoka, T. & Naitoh, Y. 1994 Numerical and experimental study of bifurcation phenomena in a finite-length Taylor–Couette system. *Proceedings of fifth International Symposium on Transport Phenomena and Dynamics of Rotating Machinery* (*ISROMAC*-5) **A,** pp. 561–572.

Taylor, G. I. 1923 Stability of a viscous fluid contained between rotating cylinders. *Philosophical Transactions of the Royal Society of London* A, **223**, 289–343.

Wimmer, M. 1976 Experiments on a viscous fluid flow between concentric rotating spheres. *Journal of Fluid Mechanics* **78,** 317–335.

Wimmer, M. 1995 An experimental investigation of Taylor vortex flow between conical cylinders. *Journal of Fluid Mechanics* **292**, 205–227.